Advanced Materials

ADVANCED MATERIALS
www.advmat.de

RESEARCH ARTICLE

Femtosecond Laser Writing of Stepwise Detachable and Biodegradable Microrobots for Adjustable Locomotion and Drug Delivery

Chen Xin[1,2] | Chenchu Zhang[3] | Yue Dai[1] | Yanlei Hu[1] | Wenji Yang[1] | Yawei Wu[1] | Liang Yang[1,4] | Hao Wu[3] | Zhaoxin Lao[3] | Sizhu Wu[3] | Xin Song[5] | Jiawen Li[1] | Zuojun Shen[6] | Shiwu Zhang[1] | Jiaru Chu[1] | Li Zhang[2] | Dong Wu[1]

[1]Institute of Humanoid Robots, Key Laboratory of Precision Scientific Instrumentation of Anhui Higher Education Institutes, Department of Precision Machinery and Precision Instrumentation, University of Science and Technology of China, Hefei, China | [2]Department of Mechanical and Automation Engineering, The Chinese University of Hong Kong, Hong Kong, China | [3]School of Mechanical Engineering, School of Microelectronics, School of Instrument Science and Opto-Electronics Engineering, Hefei University of Technology, Hefei, China | [4]Suzhou Institute for Advanced Research, University of Science and Technology of China, Suzhou, China | [5]Department of Biomedical Engineering, City University of Hong Kong, Hong Kong, China | [6]The First Affiliated Hospital of USTC, University of Science and Technology of China, Hefei, China

Correspondence: Yanlei Hu (huyl@ustc.edu.cn) | Dong Wu (dongwu@ustc.edu.cn)

Received: 9 December 2025 | **Revised:** 1 September 2026 | **Accepted:** 7 September 2026

Keywords: laser 3D printing | microrobot | targeted delivery | two-photon polymerization

ABSTRACT

Inspired by natural organisms' controllable detachment, various detachable robots have been engineered toward targeted cargo delivery and environmental sensing. However, creating stepwise detachable and degradable robots at the microscale remains challenging. Herein, we report stepwise detachable and degradable microrobots (~50 μm) fabricated from a single hydrogel using spatially graded direct laser writing (SGDLW), much smaller than previously reported detachable robots. SGDLW precisely controls local laser exposure dose, thereby programming microstructure crosslinking density, resulting in controllable cross-sectional porosity ranging from 17.6% to 37.2%, and ultimately adjusting the degradation time (from 2 min to 44 min). By encoding different local crosslinking densities, microstructures capable of single-step detachment are designed, including artificial microflowers, microdandelions, and microfish eggs. Moreover, multi-step detachment of microtrees and microdandelions can be achieved with minute-scale temporal programmability. Finally, bioinspired microrobots demonstrate promising functionalities of adjustable locomotion and drug delivery, underscoring their potential in microrobotics and targeted drug delivery.

1 | Introduction

In nature, controllable detachment behaviors can be widely observed in the plant kingdom, as exemplified by dandelion seed dispersal [1] and flower wilting [2]. These controllable separation behaviors have inspired researchers to create detachable devices [3–8]. The realization of detachable systems through mechanical structure and material design has found extensive applications in microneedle devices [9–11] and multi-functional robots [12–15]. Specifically, smart microneedle devices can be ejected from the pill and achieve digestive tract mucosa penetration, thereby enhancing macromolecular drug absorption in swine while resisting physical displacement in the gastric cavity [16]. In addition, the modularized robot can achieve locking and detaching through shape switching to facilitate cell delivery in the bile duct [17]. However, most previously reported detachable or degradable systems with structural disassembly functions are generally at the millimeter scale and often rely on multi-component or

multi-material architectures to integrate actuation, cargo loading, mechanical integrity, and triggered detachment. These designs usually require detachable joints, sacrificial interfaces, or separately assembled functional modules, which increase the overall device size and fabrication complexity. In addition, detachable systems typically perform single-step detachment, limiting their functionalities. A detailed comparison of representative detachable systems, including material composition, overall size, fabrication, actuation mode, and detachable steps, is provided in Table S1. Within this defined scope of detachable systems, the design and fabrication of stepwise detachable microrobotic structures at the microscale (~50 μm) remain challenging.

To date, various degradable materials provide the possibility to develop 3D functional microrobots with controllable detachability [18–21]. The most promising technology for processing selectively degradable materials at the microscale is direct laser writing (DLW) [22–28], which enables the construction of various complex 3D microstructures for applications in minimally invasive medical devices [29–35], bioengineering [36–38], water purification [39–41], and tunable optics [42–44]. For example, disulfide-based photoresists can undergo thiol-disulfide exchange in dithiothreitol (DTT) solutions, ultimately completing the on-demand partial degradation of dual-material microstructures fabricated by two-step DLW [45]. In addition, dual-material microscaffolds containing o-nitrobenzyl ether groups can be selectively photodegraded under 700 nm laser irradiation [46]. However, current multi-material DLW strategies still face challenges. Differences in the chemical properties of different materials lead to mismatches at microstructure interfaces. Moreover, multi-step fabrication introduces high time costs and integration difficulties into the construction of complex 3D structures. Gradient multiphoton lithography strategies have further enabled spatial modulation of material properties within a single printed structure, such as adjustable refractive index microoptics and three-dimensional microdevices for optical microscopy [47, 48]. These studies demonstrate that voxel-level control of laser exposure can provide graded structural or functional properties without changing the material formulation. However, most previous applications have focused on optical components or passive microdevices. Therefore, spatially graded DLW (SGDLW) can serve as a promising strategy for supporting the fabrication of detachable microrobotic systems.

Here, we report stepwise detachable and biodegradable microrobots (~50 μm) with shape-morphing capability in a single material via the SGDLW strategy, much smaller than previous detachable robots, which are typically millimeter-scale. SGDLW encodes spatially resolved crosslinking density within hydrogel microstructures through local control of laser exposure spacing, achieving controllable cross-sectional porosity (17.6%–37.2%) and ultimately regulating the degradation kinetics (2–44 min). Therefore, it offers the flexibility to print microrobots with stepwise detachment and degradation properties, such as artificial microflowers, dandelions, and fish eggs. Furthermore, the multi-step detachable microtree and microdandelion are verified with minute-scale temporal programmability, whereas previous works mainly achieved single-step detachment. The stepwise detachable microrobots can undergo on-demand splitting in branched channels with different widths, allowing the detached subunits to enter narrower channels. The deformable and detachable microrobots can also support adjustable drug delivery, enabling more uniform spatial distribution of the released drug. The proposed SGDLW method paves the way for the next generation of intelligent microrobots with controllable detachability and degradation properties, offering potential advantages in targeted cargo delivery in complex microenvironments.

2 | Results

2.1 | SGDLW of Stepwise Detachable and Degradable Microdandelion

Many plants in nature can release seeds to achieve their dissemination. A representative example is the dandelion, which can scatter dozens of small umbrella-shaped seeds. Inspired by this natural phenomenon, stepwise detachable and degradable microdandelions are printed using SGDLW (Figure 1a-i), where the laser scanning spacing at different positions of the microstructure can be programmed. The printed microdandelion presents reversible shape morphing between deionized (DI) water and phosphate-buffered saline (PBS) (Figure 1a-ii). When the laser power remains constant, regions with larger scanning spacing have lower crosslinking density, resulting in faster degradation. In the microdandelions fabricated by SGDLW, the scanning spacings (D) are set to 200 nm for the seeds and 500 nm for the middle junction. Thus, stepwise detachment and degradation of the microstructures are realized due to different degradation rates of different parts. The seeds of microdandelion can detach from the center through stepwise degradation (Figure 1a-iii). Eventually, these dispersed seeds can degrade over time in the enzyme solution (Figure 1a-iv). As shown in Figure 1b, SEM images before and after seed splitting are captured. Different from previously reported light-controlled dandelion-inspired polymer assemblies for aerial dispersal [49], our hydrogel microdandelion robots are designed for programmed enzymatic degradation and sequential structural detachment in liquid environments. Here, the developed hydrogel precursor with high printability has both shape-morphing and degradation capabilities and is composed of gelatin methacryloyl (GelMA), lithium phenyl-2,4,6-trimethylbenzoylphosphinate (LAP), and acrylamide (AAm) (Figure 1c). As a kind of material modified with photopolymerizable groups on natural gelatin (Figure S1), GelMA is capable of two-photon polymerization (TPP) printing [50]. LAP is a water-soluble photoinitiator with great biocompatibility to initiate monomer crosslinking [51]. AAm undergoes free-radical polymerization and helps form mechanically stable 3D hydrogel structures [52, 53]. At the locations scanned by the laser, the gel monomers are cross-linked and eventually stacked into complex 3D structures. In our study, each umbrella-like seed unit consists of eight petals (Figure S2). The microstructures can undergo reversible expansion and contraction with switching of the surrounding liquid with different ion concentrations. The reversible swelling behavior arises from the ionic-strength-dependent osmotic balance of the hydrogel network. In DI water, the low ionic strength favors water uptake and hydrogel swelling, whereas in PBS, ionic screening reduces the osmotic swelling pressure, resulting in water expulsion and contraction. Furthermore, the microdandelion can realize controllable detachment and degradation in the enzyme solution by programming different crosslinking densities.

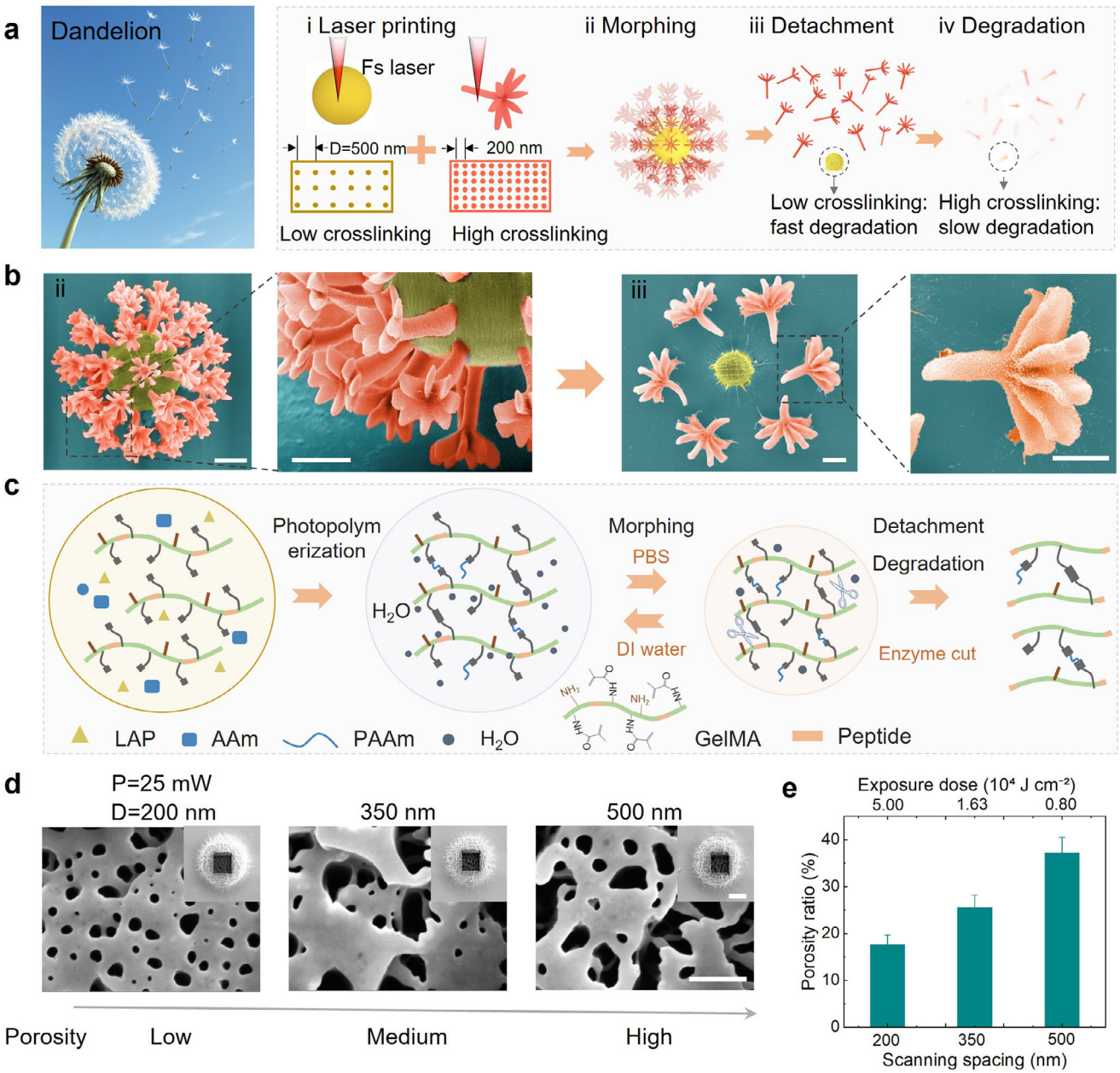

FIGURE 1 | SGDLW of stepwise detachable and degradable microdandelions. (a) Schematic illustration of the laser-printed microdandelion (i) with three programmed functions. (ii) Reversible shape-morphing of the microdandelion. (iii) Stepwise detachment of the microdandelion enabled by spatially programmed degradation. (iv) Complete degradation of the microdandelion structure under enzymatic conditions. (b) SEM images of the laser-printed microdandelion before and after detachment. (c) Main components of the hydrogel and its morphing, detachment, and degradation mechanism. (d) FIB-SEM images reveal that the 3D microstructures exhibit varying porosities due to differences in crosslinking density. (e) As the scanning spacing increases, the crosslinking density of the microstructure decreases, leading to an increase in its porosity. All error bars represent the standard deviation (n = 3). Scale bars: (b) 10 μm in (ii) and 5 μm in (iii), (d) 1 and 5 μm in the top-right inset.

Collagenase-mediated cleavage of the GelMA network progressively weakens the hydrogel, leading to structural detachment and degradation. Femtosecond laser-printed hydrogel structures are also porous, like those fabricated by ultraviolet (UV) lithography. Compared with microscale pores in hydrogel produced by UV lithography, the pores of laser-printed hydrogels are only nanoscale. Focused ion beam–scanning electron microscopy (FIB–SEM) cross-sectional analysis further confirms that the gradient-written regions exhibit different porosities in the inner region of 3D architectures (Figure 1d), with the higher scanning spacing resulting in higher porosity. The results are closely related to enzyme diffusion, degradation kinetics, structural stability, and the resulting stepwise detachment robotic behavior. Figure S3 shows that the porosity of the hydrogel surface is consistent with the internal porosity, where red regions are nanopores of the hydrogel processed by ImageJ. We find that when the scanning spacing is 200 nm, the porosity of the hydrogel is 17.6%, and when the scanning spacing is 500 nm, the porosity increases to 37.2% (Figure 1e). Therefore, the crosslinking density in different areas

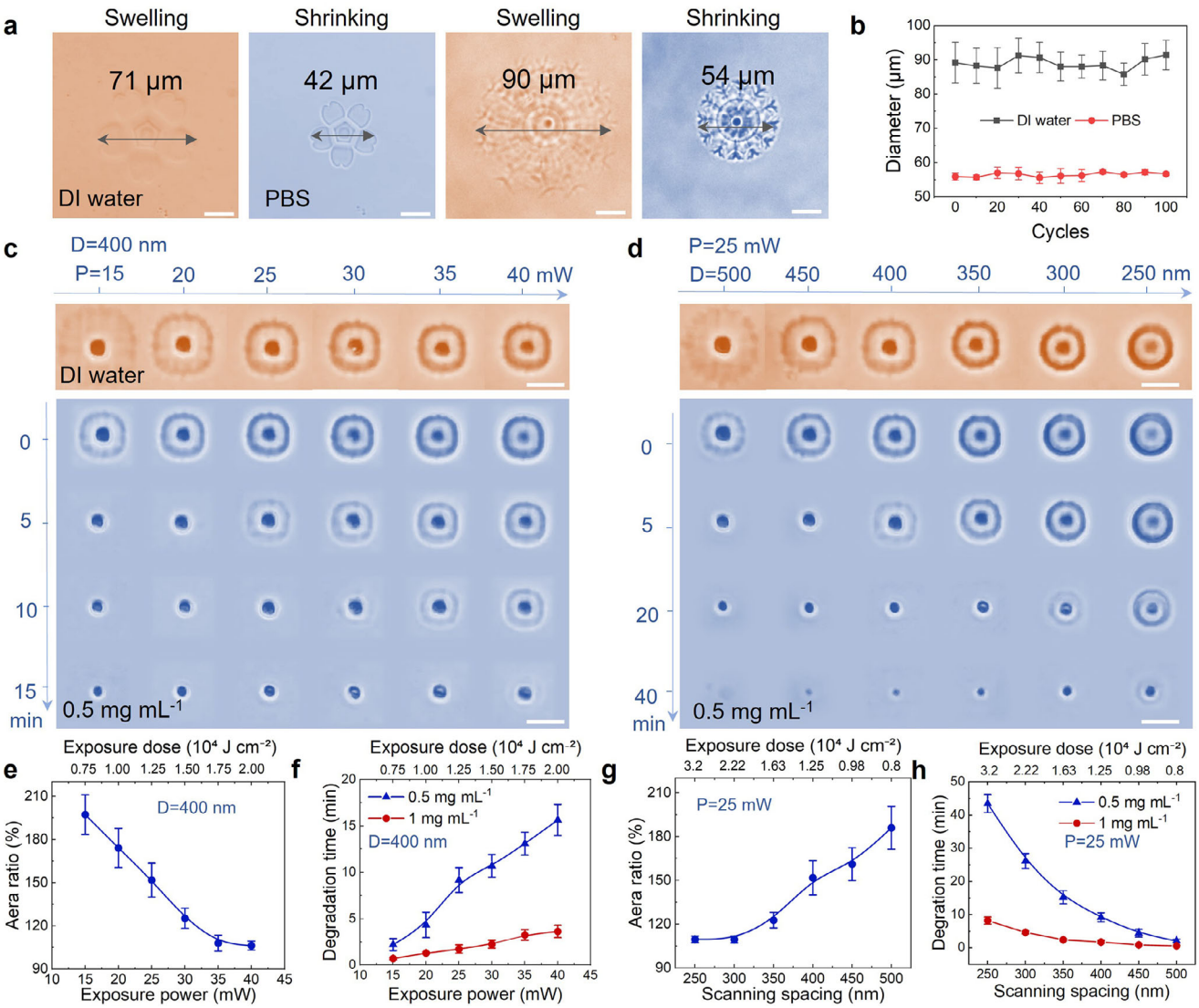

FIGURE 2 | Controllable shape morphing and degradation of microstructures. (a) Reversible shape morphing of microflower and microdandelion in DI water and PBS. (b) Quantitative analysis of the deformation amplitude over repeated cycles (right) demonstrates consistent actuation performance and good mechanical durability, indicating excellent cyclic stability of the fabricated microstructures. (c) The degradation time of microstructures can be controlled by laser exposure power. (d) The degradation time of microstructures can be controlled by scanning spacing. (e) As the exposure power increases with fixed scanning spacing (400 nm), the corresponding exposure dose increases from 0.75×10^4 to 2.00×10^4 J cm^{-2}, and the microplate area decreases during DI water due to high crosslinking density. (f) As the exposure power increases, the degradation time gradually increases correspondingly. (g) As the scanning spacing increases with fixed exposure power (25 mW), the corresponding exposure dose decreases from 3.20×10^4 to 0.80×10^4 J cm^{-2}; the microplate area increases in DI water due to low crosslinking density. (h) As the scanning spacing increases, the degradation time gradually decreases, correspondingly. All error bars represent the standard deviation ($n = 3$). Scale bars: (a) 20 μm, (c,d) 10 μm.

of the hydrogel can be adjusted by controlling the point-to-point scanning spacing of the femtosecond laser, which we call SGDLW. This printing strategy can be used to construct various detachable and degradable microstructures.

2.2 | Controllable Shape Morphing and Degradation of Microstructure

Because the nanopores inside the hydrogel are filled with a large amount of solution, an osmotic pressure difference occurs between the interior liquid of the hydrogel and the ambient liquid of the surroundings, affecting the shape and size of the structure. As shown in Figure 2a, when the hydrogel is immersed in DI water, the hydrogel is in a swollen state, and the printed microflower and microdandelion sizes reach 71 and 90 μm, respectively. When PBS is added, they shrink to 42 and 54 μm (Movie S1). Cyclic solution-switching experiments further confirm that the microstructures reversibly contract in high-ionic-concentration solution and re-expand in low-ionic-concentration solution over one hundred cycles (Figure 2b and Figure S4). Generally, the porosity of the hydrogel affected by the crosslinking degree is inversely proportional to the unit exposure dose of the laser, which is determined by the laser exposure energy and the scanning spacing. Therefore, exposure power and scanning spacing influence the hydrogel's shrinking degree

and degradation time. As shown in Figure 2c, microplates are fabricated with varying exposure power and scanning spacing to investigate their influence on degradation time. With the increase in exposure power, the microplate exhibits a smaller size after swelling while degradation time increases. When the scanning spacing increases, microplate size increases and degradation time decreases (Figure 2d). To quantitatively estimate the shape morphing, the area ratio of microplates in DI and PBS solutions is defined to characterize the morphing degree. As shown in Figure 2e, when the scanning spacing is fixed at 400 nm, the area ratio decreases from 197% to 106% with the increase of exposure power from 15 to 40 mW, and the corresponding exposure dose increases from 0.75×10^4 to 2.00×10^4 J cm^{-2}. In addition, the degradation time of the microplate increases from 2 to 16 min at an enzyme concentration of 0.5 mg mL^{-1} (Figure 2f and Table S2). When the exposure power is fixed at 25 mW, the area ratio increases from 109% to 186% with the increase of scanning spacing (250–500 nm), the corresponding exposure dose decreases from 3.20×10^4 to 8.00×10^3 J cm^{-2} (Figure 2g and Table S3). Meanwhile, the degradation time decreases from 44 to 2 min at the same enzyme concentration of 0.5 mg mL^{-1} (Figure 2h). It's worth mentioning that the degradation time decreases with increasing enzyme concentration. For example, when exposure power and scanning spacing are 25 mW and 250 nm, the full degradation time of the microplate decreases from 44 min (0.5 mg mL^{-1}) to less than 10 min (1 mg mL^{-1}, Figure S5). At a substantially lower collagenase concentration (100 ng mL^{-1}), the degradation rate of the microrobots is significantly reduced, requiring 32 h for partial degradation (Figure S6). In addition, environmental parameters, including solution composition, pH, and temperature, can influence detachment dynamics by affecting both enzyme activity and the physicochemical state of the hydrogel network. Compared with previously reported degradable microstructures based on chemical or optical triggers, our system highlights the region-programmed degradation kinetics within a single integrated hydrogel microrobot, enabling sequential multistep detachment within a controllable time window (Table S4).

2.3 | Single-Step Detachment and Degradation of Various Microstructures

Based on flexible SGDLW, controllable detachment and degradation of various microstructures can be realized. First, a microscale Great Wall is fabricated, which can gradually degrade within 20 min in an enzyme solution (Figure 3a and Figure S7). In addition to the synchronized degradation of the structure, we can also control the laser scanning spacing at different positions of the microstructure to achieve stepwise detachment and degradation. Inspired by natural dandelion spreading seeds, artificial microdandelions are fabricated with different scanning spacings at various locations, where the scanning spacing of the seeds is $D = 200$ nm, and the scanning spacing of the middle junction is 350 nm. The middle joint of the microdandelions can quickly degrade and separate into several dozens of microseeds within 4 min in the enzyme solution (Figure 3b). Subsequently, scattered microseeds with smaller scanning spacing undergo gradual degradation over 12 min. Based on the same design principle, microflowers with stepwise detachment and degradation are also developed (Figure 3c). The scanning spacings of the micropetals and central parts are $D = 200$ and 300 nm, respectively. They can first be divided into five petals via the degradation of low-crosslinking parts. After that, the detached micropetals with high crosslinking density can completely degrade within 20 min. In addition, a microfish egg cluster with controllable detachment and degradation is also developed to demonstrate the microstructure versatility of the proposed strategy (Figure 3d and Movie S2). More importantly, the above microstructure arrays with different scanning spacing designs demonstrate consistent detachment and degradation capability, presenting the robustness of our printing strategy (Figure S8). Because the detachment process relies on collagenase-mediated hydrogel degradation, the absolute detachment time should be interpreted under the defined experimental conditions and may vary with enzyme concentration, solution composition, pH, ionic strength, and temperature, whereas the relative detachment sequence is programmed by region-dependent degradation kinetics encoded through local crosslinking density.

2.4 | Multi-Step Detachment of Various Microstructures

Based on the precise control of laser scanning spacing, our microstructures achieve sequential multi-step detachment rather than relying on a single-step detachment approach. As shown in Figure 4a, we use a microtree with leaves and fruits as an example to represent this concept. The laser scanning spacing at the connection between the leaves and branches is set to 300 nm (light yellow), while the spacing at the connection between the fruit and the tree trunk is set to 250 nm (dark yellow). As a result, the leaves detach from the branches within 10 min, and after 25 min, the fruits begin to detach (Movie S3). We next design a four-region microdandelion to mimic the gradual splitting of seeds from the central region. Different laser scanning spacings, ranging from 300 to 600 nm and indicated by a dark-to-light color transition, are assigned to different regions. In this setup, the seeds in the 600 nm region detach first, while the seeds in other regions remain unchanged. After approximately 13 min, the seeds in the 300 nm region gradually complete their detachment (Figure 4b). For the four-region microdandelion, different programmed regions detach at clearly distinguishable time points, and the detachment-time distribution of each scanning-spacing level is statistically analyzed from three independent samples (Figure S9). Based on the same design principle, we further construct a dandelion array with sequential seed detachment. In this array, the dandelion seeds in the top-left corner detach first, and after 9 min, the seeds in the bottom-left corner complete the detachment process (Figure 4c). The multi-step detachment behavior is recorded by time-lapse images. For the 2×2 microdandelion arrays, the detachment onset time and completion time of each microdandelion are further quantified to evaluate array-level reproducibility (Figure 4d). Here, the onset time is defined as the first visible structural splitting event, whereas the completion time is defined as the full separation of the programmed region from the parent structure. For each processing condition, three independently fabricated microdandelion arrays are analyzed. These results support reproducible minute-scale temporal programmability rather than only average detachment timing. The results demonstrate that the proposed laser processing strategy can precisely control the order and timing of multi-step structural detachment, providing high-performance

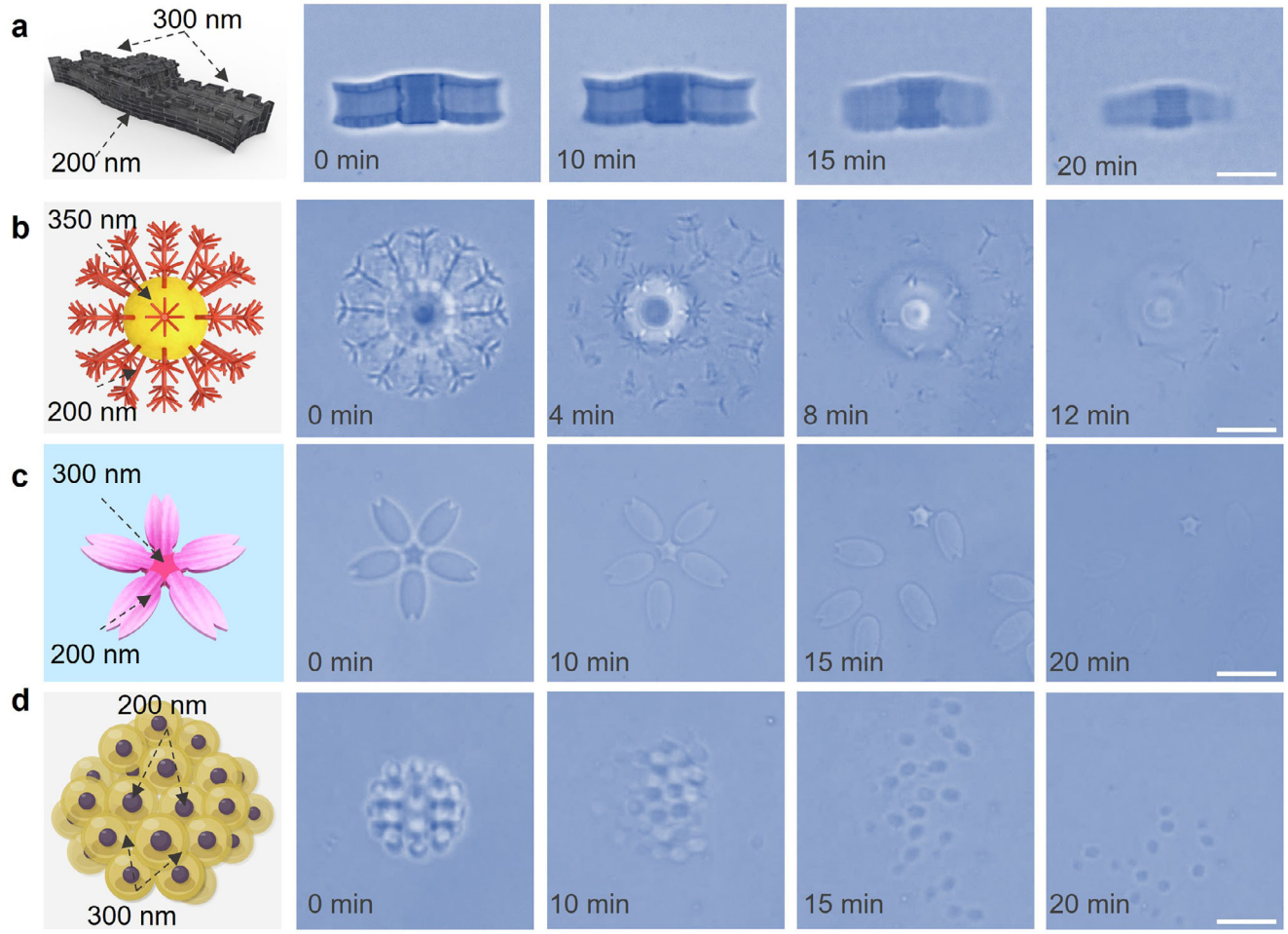

FIGURE 3 | Single-step detachment and degradation of various microstructures. (a) The microscale Great Wall degrades from both sides to the middle. (b) As natural dandelions spread their seeds, the microdandelion can detach its seeds into liquids. (c) The microflower can detach into five petals, and each petal can completely degrade over 20 min. (d) Microfish eggs can detach into dozens of individual eggs and eventually degrade over time. Three samples are made for all the microstructures. All scale bars: 20 μm.

support for applications in microrobots, microactuators, and biomedical fields.

2.5 | Magnetic Microdandelion With Stepwise Detachment for Adjustable Locomotion

To expand the application scenarios of the microstructure, magnetic nanoparticles are introduced to the surface of the microstructure for wireless precise guidance by the external dynamic magnetic field. In this study, microdandelions are immersed in Fe_3O_4 suspensions for 4 h, and their surfaces are coated with magnetic nanoparticles. Then, microdandelions are transferred to Helmholtz coils for locomotion. After Fe_3O_4 nanoparticle modification, the microrobots are washed three times with DI water/PBS to remove unbound nanoparticles, and additional 3 M adhesive tape and 30 min ultrasonic vibration tests confirm stable nanoparticle retention, indicating that nanoparticle detachment has a negligible influence on the magnetic locomotion under the tested conditions (Figure S10). Expanding locomotion modes is extremely beneficial for improving the environmental adaptability and applications of microdandelion. In our work, microdandelions can rapidly roll to the target position, and their speed and direction can also be flexibly adjusted (mode i). Subsequently, collagenase solution is added to the liquid causing the seeds to detach from the microdandelions. Detached seeds of smaller sizes can also be driven by the magnetic field (mode ii, Figure 5a). Microscope images show the corresponding states within 17 min (Figure 5b). High-magnification microscopic images further confirm that the detached Fe_3O_4-modified microseeds retain clear seed-like structural boundaries after programmed degradation-induced separation (Figure S11). Under a rotating magnetic field at different frequencies, microdandelion exhibits different propelling speeds. As shown in Figure 5c, microdandelion is propelled at 2 and 20 Hz, respectively (Movie S4). Systematic experiments reveal that the speed of microdandelions increases with the frequency increase of the magnetic field at first, and the fastest speed can reach 252 μm s^{-1}. Then the step-out frequency appears (20 Hz), and the speed of microdandelions decreases with the increase of frequency (Figure 5d and Figure S12). Compared with the microdandelions (mode i), the detached seeds (mode ii) have a much lower rolling speed under the same magnetic field. After comparative analysis, it is found that the speed of mode (i) is 7.9 times that of mode (ii) (Figure 5e). The programmed structural disassembly changes the effective size and magnetic response

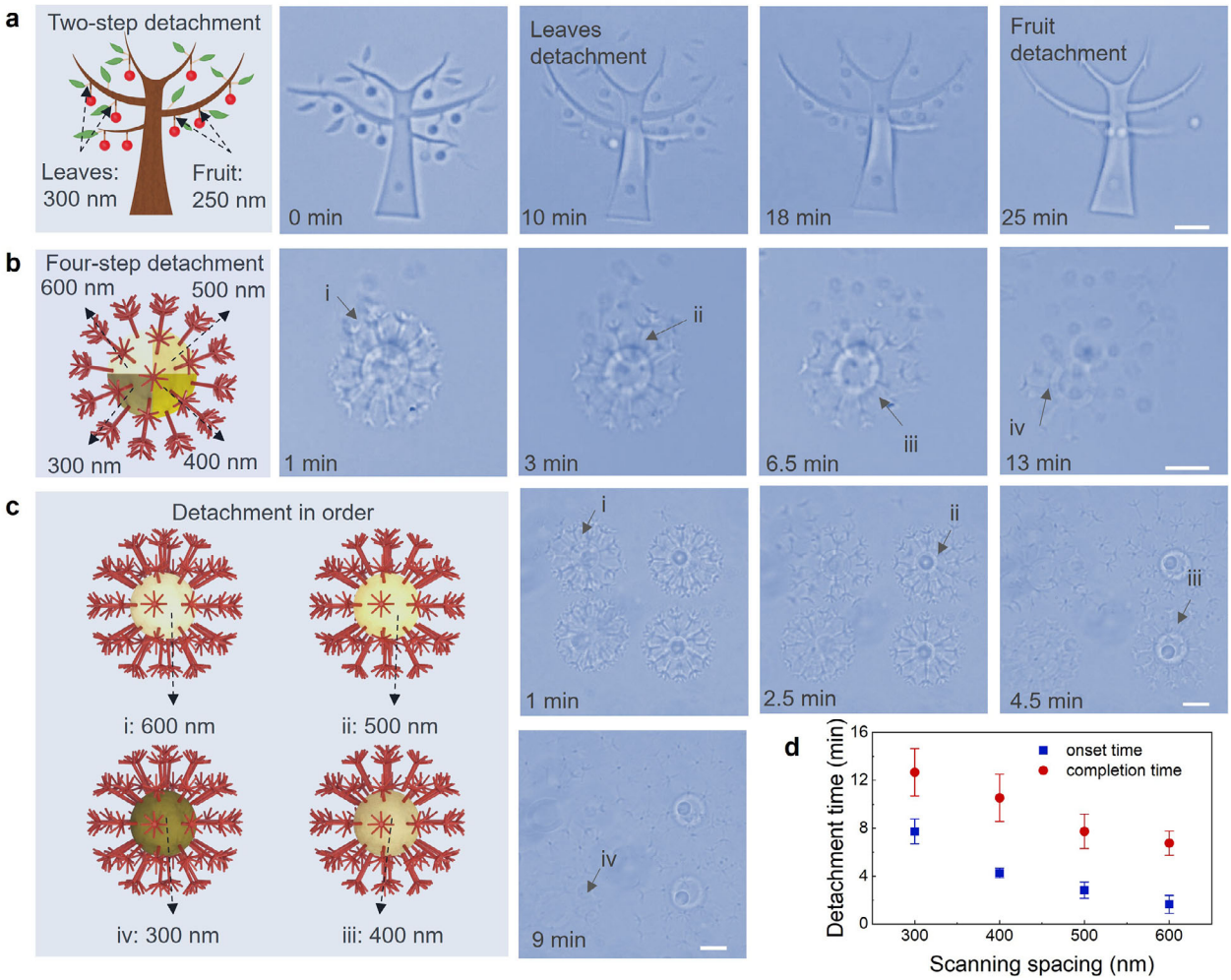

FIGURE 4 | Precise control of multi-step detachment of various microstructures. (a) Demonstration of two-step detachment of the microscale fruit tree. The leaves first detach, and the fruit second detach due to different laser scanning spacing design. (b) Demonstration of four-step detachment of microdandelion. The seeds detach in a clockwise order starting from the top-left corner. (c) Demonstration of detachment in order of a microdandelion array. The microdandelion at different positions can achieve precise seed detachment at 1, 2.5, 4.5, and 9 min, respectively. (d) Detachment onset and completion times of microdandelions fabricated with different processing parameters, showing the time window from the beginning of splitting to complete detachment. Detachment onset time refers to the first visible structural splitting event, and detachment completion time refers to complete programmed detachment. All error bars represent the standard deviation ($n = 3$). All scale bars: 20 μm.

of the microrobot, thereby leading to a transition in rolling velocity under the same magnetic actuation mode. Given that the net displacement per unit time of the microstructure based on the rolling mode is proportional to its body length [54], the microseed exhibits a lower movement speed at the same magnetic field rotation frequency. Kinematic analysis shows that larger magnetic microstructures exhibit higher translational velocities under the same rotating magnetic field, indicating a positive correlation between locomotion speed and characteristic size (Note S1). Therefore, stepwise detachable microdandelions have advantages in on-demand delivery in complex environments. To further demonstrate the functional advantage of the detachable microdandelion design in confined branched environments, a branching microfluidic channel model is fabricated with one main channel and multiple narrower side branches (Figure 5f and Movie S5). After Fe_3O_4 functionalization, the intact magnetic microdandelion can be guided along the main channel but cannot enter the narrow branch channels because of its larger parent size (Figure 5g). After programmed degradation-induced detachment, the smaller microseed subunits are able to enter the side branches and move toward the target regions, including channel i, channel ii, and channel iii (Figure 5h). This result shows that programmed detachment enables secondary access to confined branch spaces that are inaccessible to the intact microrobot, supporting its potential for localized and spatially distributed cargo delivery in branched microenvironments. It is expected that the detachable microrobot with adjustable locomotion modes can deliver cargo in micronetworks with different widths.

2.6 | Detachable Microdandelions for Adjustable Drug Delivery

In recent years, targeted drug delivery has developed rapidly. However, uneven drug delivery does remain a challenge for high therapeutic efficiency. Our proposed stepwise detachable microdandelions with shape-morphing hold promise in addressing this problem. In our study, the chemotherapeutic drug is doped into

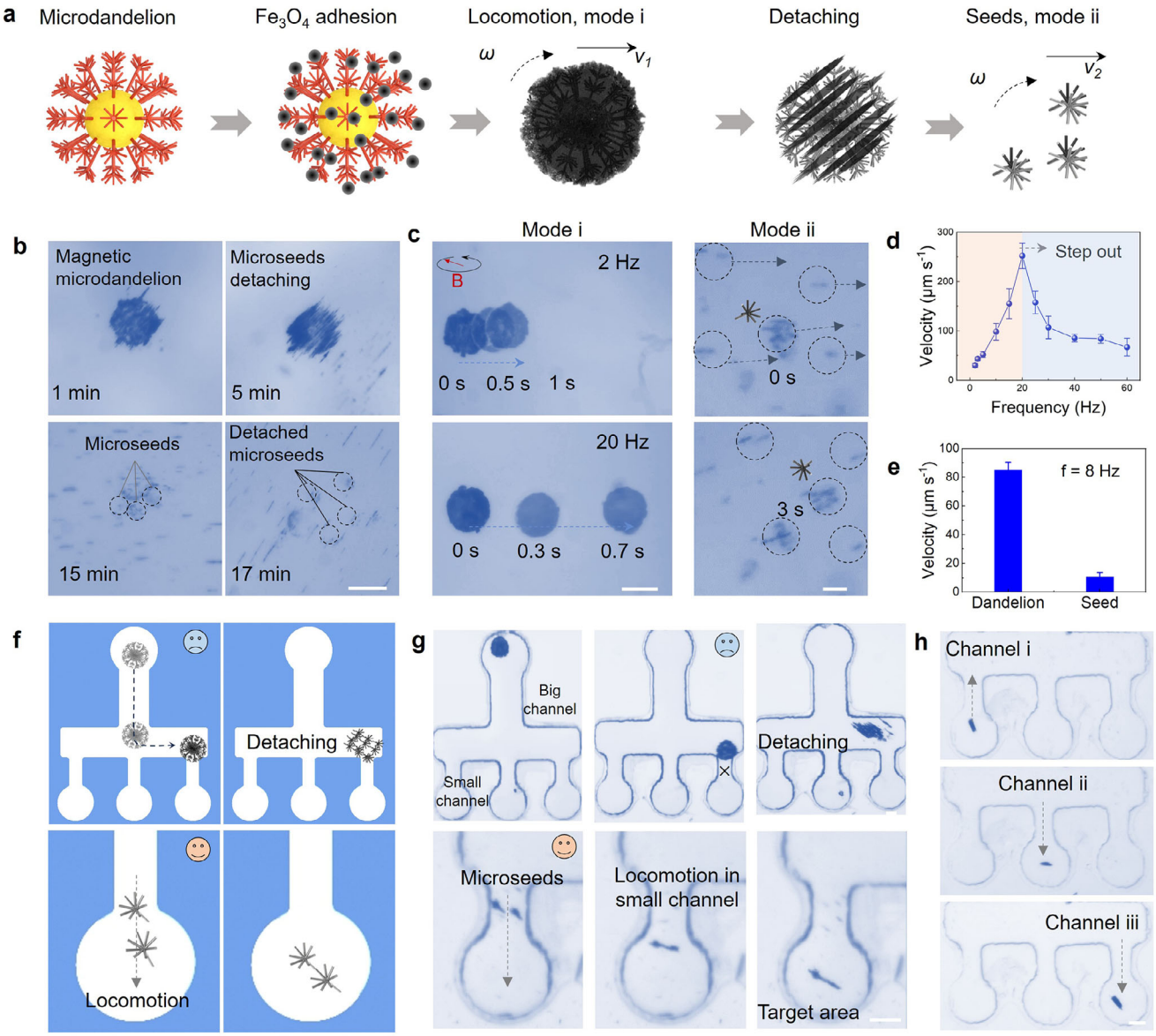

FIGURE 5 | Magnetic microdandelion with stepwise detachment and degradation for adjustable locomotion modes. (a) Schematic illustration of detachable magnetic microrobots with adjustable locomotion modes for on-demand delivery. (b) Time-lapse images of magnetic microdandelion seeds detaching in the enzyme solution. (c) Time-lapse images of microdandelion and split seeds locomotion under a rotating magnetic field. (d) The locomotion velocity as a function of rotation frequency in DI water. (e) Maximum velocity of microdandelions before and after detachment via the same magnetic field. (f,g) Schematic illustration and representative optical images showing the motion and programmed detachment of Fe_3O_4-functionalized magnetic microdandelions in a branching microfluidic channel model. Before detachment, the intact microdandelion can be magnetically guided along the main channel but is unable to enter the narrower branch channels because of its larger size. After programmed degradation-induced detachment, the smaller microseed subunits enter the branch channels and move toward the target regions. (h) The detached microseeds are able to access different branch channels, including channel i, channel ii, and channel iii. All error bars represent the standard deviation ($n = 3$). Scale bars: (b) 50 μm, (c) left, 50 μm, right, 10 μm, (f–h) 20 μm.

the hydrogel system, which can be shown by red fluorescence. For the microdandelion used in the delivery demonstration, the DOX concentration in the hydrogel precursor is 1 mg mL^{-1}, and the volume of one microdandelion is approximately 4.13 × 10^{-8} mL. Assuming homogeneous DOX distribution within the hydrogel matrix, the theoretical DOX content is estimated to be approximately 41.3 pg per microdandelion. According to the DOX release curve (Figure S13), the drug release efficiency of the hydrogel is 95.3%. Thus, the estimated drug release from a single microdandelion is 39.4 pg. Microdandelion utilizes contraction and degradation to achieve dual-mode drug delivery (mode i: rapid and mode ii: dispersive, Figure 6a and Figure S14). When the dandelions contract, the drug is rapidly released, causing the red fluorescence intensity to decrease. The quantitative analysis shows that when the hydrogel shrinks and squeezes out the internal water, the fluorescence area and average fluorescence intensity are reduced (Figure S15). In addition to rapid delivery, microdandelion can also use stepwise detachment and degradation to realize dispersive drug delivery. Driven by a dynamic magnetic field, the microdandelion can achieve targeted

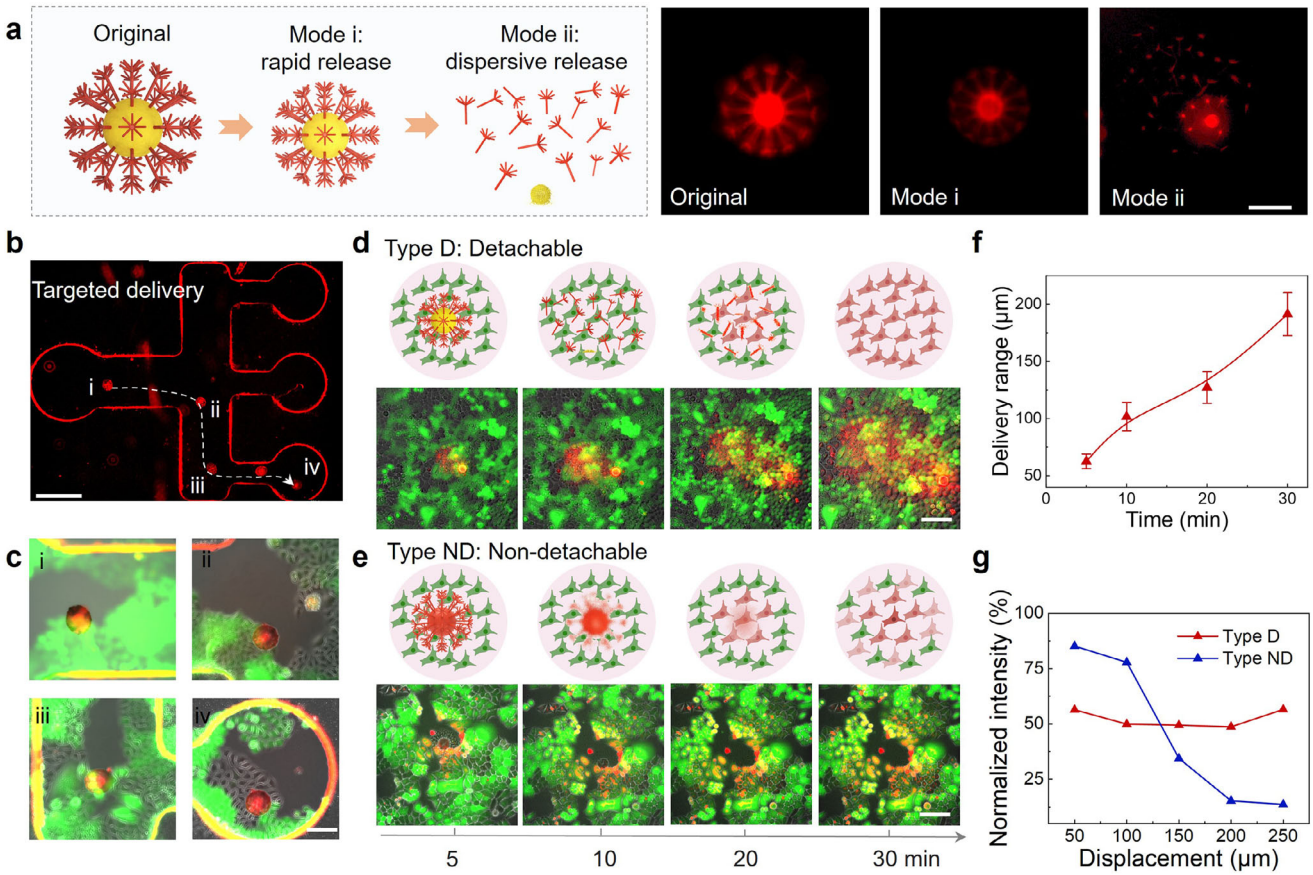

FIGURE 6 | Detachable microdandelions for adjustable drug delivery. (a) Rapid (mode i) and dispersive drug delivery (mode ii) of microdandelions are achieved by their contraction and degradation. (b) The microdandelion can achieve targeted delivery in specific areas in microchannels filled with cells. (c) The enlarged images at four locations from i to iv. (d~e) Comparison of drug delivery through detachable dandelion (type: D) and nondetachable dandelion (type: ND). Type D can achieve more uniform drug delivery based on seed detachment. (**f**) Dispersive drug delivery is realized by detachable microdandelion. The relationship between microseed dispersal range and time is shown. (g) Comparison of drug delivery uniformity of microdandelions with and without seed detachment. All error bars represent the standard deviation ($n = 3$). Scale bars: (a) 50 μm, (b) 500 μm, and (c–e) 100 μm.

delivery to specific areas in a microchannel cultured with cells (Figure 6b). The enlarged images at four locations (i–iv) prove that the microdandelion has good adaptivity and accessibility (Figure 6c). Detachable microdandelion (type D) can achieve dispersive drug delivery with a uniform dose (Figure 6d). In contrast, nondetachable microdandelion (type ND) makes it difficult to achieve uniform drug delivery (Figure 6e). Over 30 min, the fluorescent seed is about 200 μm away from the original center to realize uniform drug delivery (Figure 6f and Figure S16). As shown in Figure 6g, in type ND, cancer cells close to the microdandelion show stronger red drug fluorescence. The farther away from the microdandelion, the weaker the red fluorescence exhibited by the cells, reflecting the inhomogeneity of drug delivery. In contrast, in type D, microdandelion can be split into dozens of seeds, showing a more uniform cancer cell treatment. Notably, collagenase and microdandelion show good biological safety and do not have toxic side effects on cells (Figure S17). In addition to fluorescence intensity alone, CCK-8 cell viability assays and Calcein-AM/PI live/dead staining are performed, confirming that DOX-loaded microrobots significantly reduce HeLa cell viability and induce measurable cytotoxicity (Figure S18). Therefore, stepwise detachable and degradable microstructures may provide a promising platform for dual-mode drug delivery to achieve uniform treatment. The application of microrobots in drug delivery can be further advanced by integrating them with magnetic field generation systems used in clinical trials [55].

3 | Discussion

We have proposed a strategy for constructing microrobots that can detach step by step at the micrometer scale (~50 μm), much smaller than most previous detachable robots (> 1 mm) that only allow single-step detachment. However, current research is still in its early stages, and there is still much space for improvement. Because enzymatic degradation is not intrinsically temporally or spatially selective, premature degradation and drug leakage during targeting remain important concerns; future designs should reduce leakage by optimizing local crosslinking density, introducing protective or diffusion-barrier layers, strengthening drug–matrix interactions, or incorporating target-specific enzymatic/external triggering mechanisms. The single-material, multi-step splitting strategy may be particularly useful for future targeted delivery in confined and branched luminal environments. A parent microdandelion can first be magnetically guided to a target region and then split into smaller subunits through programmed degradation. This progressive size

reduction may allow the detached subunits to access narrower regions, such as biliary ducts or vascular side branches, that are difficult for the parent structure to enter. Moreover, the generation of multiple smaller subunits may enable more spatially distributed local cargo release rather than release from a single point. Therefore, the potential value of this platform lies not only in miniaturization, but also in programmable structural transformation, secondary access after detachment, and spatially distributed release. Future work will need to further evaluate cargo loading capacity, release efficiency, premature leakage, physiological degradation kinetics, magnetic control in anatomical and flow environments, biosafety, and therapeutic efficacy in more realistic models. In particular, animal studies will be necessary to determine whether the programmed detachment, magnetic navigation, drug release, and degradation observed in vitro can be maintained under complex physiological conditions.

In summary, we present the development of stepwise detachable and degradable microrobots utilizing SGDLW in a single hydrogel. The programmable crosslinking density by laser exposure control leads to multi-step detachment and degradation of microrobots, whereas most previously reported detachable robots can only exhibit single-step detachment. Moreover, stepwise detachable microrobots exhibit promising performance in the realms of microrobotics and drug delivery. Detachable magnetic microrobots show adjustable-mode locomotion with different speeds to meet requirements in various applications. In addition, dual-mode drug delivery is demonstrated by microdandelions with detachable seeds, offering the potential for improved cancer cell treatment. These results suggest that detachable and degradable microrobots can serve as a new tool in the fields of microrobotics and biomedicine.

4 | Materials And Methods

4.1 | Materials

GelMA was synthesized as described before [56], where the degree of methacrylation of the synthesized GelMA was calculated to be approximately 85.1% (Figure S19). The photoinitiator LAP was purchased from Macklin. Doxorubicin hydrochloride (DOX), AAm, PBS, and collagenase were purchased from Aladdin. Fe_3O_4 NPs (~200 nm) were purchased from Sigma. All chemicals were used directly as received.

4.2 | Hydrogel Synthesis

15 mg LAP and 5 mg AAm were added to 1 mL PBS. The mixer was ultrasonically mixed at 40°C. Then, 150 mg GelMA was added to the solution, followed by stirring for 1 h to ensure the complete mixing of each component in the solution. DOX was added to the above hydrogel (1 mg mL^{-1}) to encapsulate DOX in the microstructure. Once made, the precursor was kept in yellow light conditions to prevent unnecessary exposure. DOX, a fluorescent model anticancer drug, was incorporated into the hydrogel precursor to demonstrate cargo loading, degradation-associated release, and preliminary cytotoxic effects on HeLa cells [57].

4.3 | Direct Laser Writing of Hydrogel and Characterization

Before printing the hydrogel, it is necessary to place the hydrogel in warm water at 50°C to form a flowable liquid and then transfer 15 μL of the hydrogel to a clean coverslip with a micropipette. A typical femtosecond laser writing system source is a mode-locked Ti: sapphire laser oscillator (Chameleon Vision-S, Coherent Corp). The structures were written using a 780 nm femtosecond laser through a 60× oil-immersion objective with NA = 1.35. The laser repetition rate was 80 MHz, the pulse duration was 75 fs, the optical-path transmittance to the sample plane was estimated as 0.8, and the effective exposure time per spot was 1 ms. First, processing was performed using femtosecond laser direct writing technology. The polymer molecular chains at the laser focus were polymerized. The processed sample was immersed in a developing solution (DI water) for 15 min at 50°C to remove the uncured hydrogel. The developed sample was then taken out and placed under an inverted microscope for in situ observation. When PBS solution was dropped, the sample shrunk, and then it was transferred to DI water to make the microstructure swell.

4.4 | Preparation of Magnetic Microdandelion and Its Magnetic Propelling

After 4D printing, the sample was immersed in the magnetic particles (Fe_3O_4 NPs) suspension for 4 h to absorb nanoparticles. Subsequently, we used a homemade three-dimensional mobile platform and capillary microneedle to peel off the microrobot and transfer it with a microliter pipette. After Fe_3O_4 nanoparticle modification, the microrobots were washed three times with DI water/PBS to remove unbound nanoparticles, and additional 3 M adhesive tape and 30 min ultrasonic vibration tests confirmed stable nanoparticle retention, indicating that possible nanoparticle detachment had negligible influence on the observed magnetic locomotion under the tested conditions. At last, magnetic actuation of microdandelions was realized by a 3D Helmholtz coil system.

4.5 | Characterization

Optical micrographs are taken with an inverted fluorescence microscope (Leica DMI3000b). The SEM images are collected with a secondary electron SEM (ZEISS EVO18) operated at an accelerating voltage of 10 kV after depositing ~5 nm gold. All microstructures were subjected to CO_2 critical drying (EM CPD300, Leica), and their internal porosity was characterized by FIB-SEM (Helios NanoLab650).

4.6 | Cell Culture and Treatment

HeLa-EGFP cells were obtained from Shanghai Priman Biotechnology (China) and cultured in a humidified incubator at 37°C and 5% CO_2. The cells were maintained in DMEM (Gibco, Thermo Fisher Scientific, USA) supplemented with 10% fetal bovine serum (FBS; HyClone) and 1% penicillin streptomycin (Gibco). For single-cell manipulation experiments, the cells were

detached via 0.25% Trypsin-EDTA (Gibco) at 37°C for 30 s. The cell suspension was subsequently centrifuged at 150 × g for 5 min and resuspended in fresh medium to the desired density. For DOX release quantification, DOX-loaded hydrogel structures were incubated in 100 μL of release medium. The released DOX concentration was measured using a multimode microplate reader (SpectraMax iD5) in fluorescence mode. A DOX standard curve was prepared in the same release medium, and the fluorescence intensity of blank hydrogel structures was used for background subtraction. The released DOX concentration was calculated from the calibration curve ($Y = 107039X + 2875$), where (Y) represents fluorescence intensity and (X) represents DOX concentration in μg mL^{-1} (Figure S13). The release efficiency was calculated by normalizing the measured released DOX amount to the theoretical DOX loading amount estimated from the hydrogel volume and the initial DOX concentration in the precursor solution. Red fluorescence represents DOX excited by green light, while green fluorescence represents the intrinsic GFP signal of HeLa cells excited by blue light.

Author Contributions

C. X. conceived the idea and designed the project. C. X., C. Z., W. Y., Y. D., and Y.W. performed all the experiments and the characterization. C.X., C. Z., and Y.D. completed data analysis and figure preparation. H. W., Z. L., S. Z., X. S., Z. S., S. W., J. L., J. C., and L. Z. provided constructive suggestions for the results and discussion. Y. H. and D. W. mentored the work and revised the manuscript. All authors wrote and revised the paper. C.X. and C.Z. contributed equally to this work.

Funding

This work was supported by the National Natural Science Foundation of China (Nos. 52375582, 62275242, 62461160305, 62475066), Major Scientific and Technological Projects in Anhui Province (202203a05020014), Suzhou Innovation Youth Leading Talent Project (ZXL2023158), the Fundamental Research Funds for the Central Universities (YD2090002019, YD2090002005, WK2090050048, WK2090000001), USTC Research Funds of the Double First-Class Initiative (YD2095202609), and Youth Innovation Promotion Association CAS (Y2021118). L.Z. thanks the financial support from the Hong Kong Research Grants Council (RGC) with project No. N_CUHK472/24. We acknowledge the Experimental Center of Engineering and Material Sciences at USTC for the fabrication and measurement of samples. This work was partly carried out at the USTC Center for Micro and Nanoscale Research and Fabrication.

Conflicts of Interest

The authors declare no conflicts of interest.

Data Availability Statement

The data that support the findings of this study are available from the corresponding author upon reasonable request.

References

1. C. Cummins, M. Seale, A. Macente, et al., "A Separated Vortex Ring Underlies the Flight of the Dandelion," *Nature* 562 (2018): 414–418, https://doi.org/10.1038/s41586-018-0604-2.

2. S. Reichardt, H.-P. Piepho, A. Stintzi, and A. Schaller, "Peptide Signaling for Drought-Induced Tomato Flower Drop," *Science* 367 (2020): 1482–1485, https://doi.org/10.1126/science.aaz5641.

3. M. Rubenstein, A. Cornejo, and R. Nagpal, "Programmable Self-Assembly in a Thousand-Robot Swarm," *Science* 345 (2014): 795–799, https://doi.org/10.1126/science.1254295.

4. L. Huang, L. Li, Y. Jiang, et al., "Tumbler-Inspired Microneedle Containing Robots: Achieving Rapid Self-Orientation and Peristalsis-Resistant Adhesion for Colonic Administration," *Advanced Functional Materials* 33 (2023): 2304276, https://doi.org/10.1002/adfm.202304276.

5. K. Lee, H. B. Song, W. Cho, J. H. Kim, J. H. Kim, and W. Ryu, "Intracorneal Injection of a Detachable Hybrid Microneedle for Sustained Drug Delivery," *Acta Biomaterialia* 80 (2018): 48–57, https://doi.org/10.1016/j.actbio.2018.09.039.

6. S. Li, R. Batra, D. Brown, et al., "Particle Robotics Based on Statistical Mechanics of Loosely Coupled Components," *Nature* 567 (2019): 361–365, https://doi.org/10.1038/s41586-019-1022-9.

7. Z. Yang, L. Yang, M. Zhang, N. Xia, and L. Zhang, "Ultrasound-Guided Wired Magnetic Microrobot With Active Steering and Ejectable Tip," *IEEE Transactions on Industrial Electronics* 70 (2022): 614–623, https://doi.org/10.1109/TIE.2022.3153809.

8. A. Abramson, E. Caffarel-Salvador, V. Soares, et al., "A Luminal Unfolding Microneedle Injector for Oral Delivery of Macromolecules," *Nature Medicine* 25 (2019): 1512–1518, https://doi.org/10.1038/s41591-019-0598-9.

9. W. Li, R. N. Terry, J. Tang, M. R. Feng, S. P. Schwendeman, and M. R. Prausnitz, "Rapidly Separable Microneedle Patch for the Sustained Release of a Contraceptive," *Nature Biomedical Engineering* 3 (2019): 220–229, https://doi.org/10.1038/s41551-018-0337-4.

10. A. Than, C. Liu, H. Chang, et al., "Self-Implantable Double-Layered Micro-Drug-Reservoirs for Efficient and Controlled Ocular Drug Delivery," *Nature Communications* 9 (2018): 4433, https://doi.org/10.1038/s41467-018-06981-w.

11. H. Chang, S. W. T. Chew, M. Zheng, et al., "Cryomicroneedles for Transdermal Cell Delivery," *Nature Biomedical Engineering* 5 (2021): 1008–1018, https://doi.org/10.1038/s41551-021-00720-1.

12. Y. Liang, Y. Xu, W. Ye, D. Yao, Y. Chen, and C. Wang, "Multi-Stage Hydrogel Rockets With Stage Dropping-Off by Thermal/Light Stimulation," *Journal of Materials Chemistry A* 6 (2018): 16838–16843, https://doi.org/10.1039/C8TA06715E.

13. X. Yang, R. Tan, H. Lu, T. Fukuda, and Y. Shen, "Milli-Scale Cellular Robots That Can Reconfigure Morphologies and Behaviors Simultaneously," *Nature Communications* 13 (2022): 4156, https://doi.org/10.1038/s41467-022-31913-0.

14. K. Lee, Y. Xue, J. Lee, et al., "A Patch of Detachable Hybrid Microneedle Depot for Localized Delivery of Mesenchymal Stem Cells in Regeneration Therapy," *Advanced Functional Materials* 30 (2020): 2000086, https://doi.org/10.1002/adfm.202000086.

15. C. Xin, N. Xia, and L. Zhang, "Light-Based 3D Printing of Stimulus-Responsive Hydrogels for Miniature Devices: Recent Progress and Perspective," *Bio-Design and Manufacturing* 7 (2024): 721–746, https://doi.org/10.1007/s42242-024-00295-1.

16. W. Chen, J. Wainer, S. W. Ryoo, et al., "Dynamic Omnidirectional Adhesive Microneedle System for Oral Macromolecular Drug Delivery," *Science Advances* 8 (2022): abk1792, https://doi.org/10.1126/sciadv.abk1792.

17. L. Su, D. Jin, Y. Wang, et al., "Modularized Microrobot With Lock-and-Detachable Modules for Targeted Cell Delivery in Bile Duct," *Science Advances* 9 (2023): adj0883, https://doi.org/10.1126/sciadv.adj0883.

18. D. Gräfe, A. Wickberg, M. M. Zieger, M. Wegener, E. Blasco, and C. Barner-Kowollik, "Adding Chemically Selective Subtraction to Multi-Material 3D Additive Manufacturing," *Nature Communications* 9 (2018): 2788, https://doi.org/10.1038/s41467-018-05234-0.

19. X. Wang, X.-H. Qin, C. Hu, et al., "3D Printed Enzymatically Biodegradable Soft Helical Microswimmers," *Advanced Functional Materials* 28 (2018): 1804107, https://doi.org/10.1002/adfm.201804107.

20. H. Ceylan, N. O. Dogan, I. C. Yasa, M. N. Musaoglu, Z. U. Kulali, and M. Sitti, "3D Printed Personalized Magnetic Micromachines From Patient Blood–Derived Biomaterials," *Science Advances* 7 (2021): abh0273, https://doi.org/10.1126/sciadv.abh0273.

21. M. Gernhardt, V. X. Truong, and C. Barner-Kowollik, "Visible-Light-Degradable 3D Microstructures in Aqueous Environments," *Advanced Materials* 34 (2022): 2203474.

22. C. Xin, D. Jin, Y. Hu, et al., "Environmentally Adaptive Shape-Morphing Microrobots for Localized Cancer Cell Treatment," *ACS Nano* 15 (2021): 18048–18059, https://doi.org/10.1021/acsnano.1c06651.

23. L. Zhang, B. Liu, C. Wang, et al., "Functional Shape-Morphing Microarchitectures Fabricated by Dynamic Holographically Shifted Femtosecond Multifoci," *Nano Letters* 22 (2022): 5277–5286, https://doi.org/10.1021/acs.nanolett.2c01178.

24. C. Deng, Y. Liu, X. Fan, et al., "Femtosecond Laser 4D Printing of Light-Driven Intelligent Micromachines," *Advanced Functional Materials* 33 (2023): 2211473, https://doi.org/10.1002/adfm.202211473.

25. H. Ceylan, I. C. Yasa, O. Yasa, A. F. Tabak, J. Giltinan, and M. Sitti, "3D-Printed Biodegradable Microswimmer for Theranostic Cargo Delivery and Release," *ACS Nano* 13 (2019): 3353–3362, https://doi.org/10.1021/acsnano.8b09233.

26. Y. Bao, N. Paunović, and J. C. Leroux, "Challenges and Opportunities in 3D Printing of Biodegradable Medical Devices by Emerging Photopolymerization Techniques," *Advanced Functional Materials* 32 (2022): 2109864, https://doi.org/10.1002/adfm.202109864.

27. H. Wang, W. Zhang, D. Ladika, et al., "Two-Photon Polymerization Lithography for Optics and Photonics: Fundamentals, Materials, Technologies, and Applications," *Advanced Functional Materials* 33 (2023): 2214211, https://doi.org/10.1002/adfm.202214211.

28. Y.-L. Zhang, Y. Tian, H. Wang, et al., "Dual-3D Femtosecond Laser Nanofabrication Enables Dynamic Actuation," *ACS Nano* 13 (2019): 4041–4048, https://doi.org/10.1021/acsnano.8b08200.

29. X. Wang, X.-Z. Chen, C. C. J. Alcântara, et al., "MOFBOTS: Metal–Organic-Framework-Based Biomedical Microrobots," *Advanced Materials* 31 (2019): 1901592, https://doi.org/10.1002/adma.201901592.

30. U. Bozuyuk, O. Yasa, I. C. Yasa, H. Ceylan, S. Kizilel, and M. Sitti, "Light-Triggered Drug Release From 3D-Printed Magnetic Chitosan Microswimmers," *ACS Nano* 12 (2018): 9617–9625, https://doi.org/10.1021/acsnano.8b05997.

31. J. Park, C. Jin, S. Lee, J.-Y. Kim, and H. Choi, "Magnetically Actuated Degradable Microrobots for Actively Controlled Drug Release and Hyperthermia Therapy," *Advanced Healthcare Materials* 8 (2019): 1900213, https://doi.org/10.1002/adhm.201900213.

32. Y. Li, D. Dong, Y. Qu, et al., "A Multidrug Delivery Microrobot for the Synergistic Treatment of Cancer," *Small* 19 (2023): 2301889, https://doi.org/10.1002/smll.202301889.

33. H. Han, X. Ma, W. Deng, et al., "Imaging-Guided Bioresorbable Acoustic Hydrogel Microrobots," *Science Robotics* 9 (2024): adp3593, https://doi.org/10.1126/scirobotics.adp3593.

34. F. C. Landers, V. Gantenbein, L. Hertle, et al., "On-Command Disassembly of Microrobotic Superstructures for Transport and Delivery of Magnetic Micromachines," *Advanced Materials* 36 (2024): 2310084, https://doi.org/10.1002/adma.202310084.

35. C. Xin, Y. Wang, Y. Jiang, et al., "Ultrasound-Sensitive Microrobotic Sensor With Robust Anchoring for Long-Term Digestive Lesion Assessment," *National Science Review* 13 (2026): nwag179, https://doi.org/10.1093/nsr/nwag179.

36. M. Hippler, E. D. Lemma, S. Bertels, et al., "3D Scaffolds to Study Basic Cell Biology," *Advanced Materials* 31 (2019): 1808110, https://doi.org/10.1002/adma.201808110.

37. M. Dong, X. Wang, X.-Z. Chen, et al., "3D-Printed Soft Magnetoelectric Microswimmers for Delivery and Differentiation of Neuron-Like Cells," *Advanced Functional Materials* 30 (2020): 1910323, https://doi.org/10.1002/adfm.201910323.

38. S. Noh, S. Jeon, E. Kim, et al., "A Biodegradable Magnetic Microrobot Based on Gelatin Methacrylate for Precise Delivery of Stem Cells With Mass Production Capability," *Small* 18 (2022): 2107888, https://doi.org/10.1002/smll.202107888.

39. S. R. Dabbagh, M. R. Sarabi, M. T. Birtek, S. Seyfi, M. Sitti, and S. Tasoglu, "3D-Printed Microrobots From Design to Translation," *Nature Communications* 13 (2022): 5875, https://doi.org/10.1038/s41467-022-33409-3.

40. B. Khezri, K. Villa, F. Novotný, Z. Sofer, and M. Pumera, "Smartdust 3D-Printed Graphene-Based Al/Ga Robots for Photocatalytic Degradation of Explosives," *Small* 16 (2020): 2002111, https://doi.org/10.1002/smll.202002111.

41. J. Li and M. Pumera, "3D Printing of Functional Microrobots," *Chemical Society Reviews* 50 (2021): 2794–2838, https://doi.org/10.1039/D0CS01062F.

42. B. Liu, B. Dong, C. Xin, et al., "4D Direct Laser Writing of Submerged Structural Colors at the Microscale," *Small* 19 (2023): 2204630, https://doi.org/10.1002/smll.202204630.

43. Z. C. Ma, X. Y. Hu, Y. L. Zhang, et al., "Smart Compound Eyes Enable Tunable Imaging," *Advanced Functional Materials* 29 (2019): 1903340.

44. D. Gonzalez-Hernandez, S. Varapnickas, A. Bertoncini, C. Liberale, and M. Malinauskas, "Micro-Optics 3D Printed via Multi-Photon Laser Lithography," *Advanced Optical Materials* 11 (2022): 2201701, https://doi.org/10.1002/adom.202201701.

45. M. M. Zieger, P. Mueller, A. S. Quick, M. Wegener, and C. Barner-Kowollik, "Cleaving Direct-Laser-Written Microstructures on Demand," *Angewandte Chemie International Edition* 56 (2017): 5625–5629, https://doi.org/10.1002/anie.201701593.

46. R. Batchelor, T. Messer, M. Hippler, et al., "Two in One: Light as a Tool for 3D Printing and Erasing at the Microscale," *Advanced Materials* 31 (2019): 1904085.

47. G. Zyla, G. Maconi, A. Nolvi, et al., "3D Micro-Devices for Enhancing the Lateral Resolution in Optical Microscopy," *Light: Advanced Manufacturing* 5 (2024): 1, https://doi.org/10.37188/lam.2024.019.

48. D. Gonzalez-Hernandez, B. Sanchez-Padilla, D. Gailevicius, et al., "Single-Step 3D Printing of Micro-Optics With Adjustable Refractive Index by Ultrafast Laser Nanolithography," *Advanced Optical Materials* 11 (2023): 2300258, https://doi.org/10.1002/adom.202300258.

49. J. Yang, H. Zhang, A. Berdin, W. Hu, and H. Zeng, "Dandelion-Inspired, Wind-Dispersed Polymer-Assembly Controlled by Light," *Advanced Science* 10 (2023): 2206752, https://doi.org/10.1002/advs.202206752.

50. Y. Dong, L. Wang, V. Iacovacci, X. Wang, L. Zhang, and B. J. Nelson, "Magnetic Helical Micro-/Nanomachines: Recent Progress and Perspective," *Matter* 5 (2022): 77–109, https://doi.org/10.1016/j.matt.2021.10.010.

51. H. Montazerian, A. Baidya, R. Haghniaz, et al., "Stretchable and Bioadhesive Gelatin Methacryloyl-Based Hydrogels Enabled by In Situ Dopamine Polymerization," *ACS Applied Materials & Interfaces* 13 (2021): 40290–40301, https://doi.org/10.1021/acsami.1c10048.

52. R. Li, D. Jin, D. Pan, et al., "Stimuli-Responsive Actuator Fabricated by Dynamic Asymmetric Femtosecond Bessel Beam for In Situ Particle and Cell Manipulation," *ACS Nano* 14 (2020): 5233–5242, https://doi.org/10.1021/acsnano.0c00381.

53. C. Xin, Z. Ren, L. Zhang, et al., "Light-Triggered Multi-Joint Microactuator Fabricated by Two-in-One Femtosecond Laser Writing," *Nature Communications* 14 (2023): 4273, https://doi.org/10.1038/s41467-023-40038-x.

54. W. Hu, G. Z. Lum, M. Mastrangeli, and M. Sitti, "Small-scale Soft-bodied Robot With Multimodal Locomotion," *Nature* 554 (2018): 81–85, https://doi.org/10.1038/nature25443.

55. F. C. Landers, L. Hertle, V. Pustovalov, et al., "Clinically Ready Magnetic Microrobots for Targeted Therapies," *Science* 390 (2025): 710–715, https://doi.org/10.1126/science.adx1708.

56. A. I. Van Den Bulcke, B. Bogdanov, N. De Rooze, et al., "Structural and Rheological Properties of Methacrylamide Modified Gelatin Hydrogels," *Biomacromolecules* 1 (2000): 31.

57. S. Li, Y. Zhang, S.-H. Ho, et al., "Combination of Tumour-Infarction Therapy and Chemotherapy via the Co-Delivery of Doxorubicin and Thrombin Encapsulated in Tumour-Targeted Nanoparticles," *Nature Biomedical Engineering* 4 (2020): 732–742, https://doi.org/10.1038/s41551-020-0573-2.

Supporting Information

Additional supporting information can be found online in the Supporting Information section.

Supporting File 1: adma75013-sup-0001-SuppMat.pdf.

Supporting File 2: adma75013-sup-0002-MovieS1-S5.zip.